

NJC

Accepted Manuscript



This is an *Accepted Manuscript*, which has been through the Royal Society of Chemistry peer review process and has been accepted for publication.

Accepted Manuscripts are published online shortly after acceptance, before technical editing, formatting and proof reading. Using this free service, authors can make their results available to the community, in citable form, before we publish the edited article. We will replace this *Accepted Manuscript* with the edited and formatted *Advance Article* as soon as it is available.

You can find more information about *Accepted Manuscripts* in the [Information for Authors](#).

Please note that technical editing may introduce minor changes to the text and/or graphics, which may alter content. The journal's standard [Terms & Conditions](#) and the [Ethical guidelines](#) still apply. In no event shall the Royal Society of Chemistry be held responsible for any errors or omissions in this *Accepted Manuscript* or any consequences arising from the use of any information it contains.

ARTICLE

Polyhedral Fe₃O₄ nanoparticles for lithium ion storage

Cite this: DOI: 10.1039/x0xx00000x

Chaolun Liang,^{ab} Senchuan Huang,^a Wenxia Zhao,^b Wenyue Liu,^a Jian Chen,^b Hong Liu,^{*c} and Yexiang Tong^{*a}

Received 00th January 2012,

Accepted 00th January 2012

DOI: 10.1039/x0xx00000x

www.rsc.org/

Ferroferric oxide, Fe₃O₄, is a highly promising anode material for Lithium-ion batteries (LIBs) due to its excellent electrochemical properties. Here, by using high resolution transmission electron microscopy (HRTEM), we are able to correlate the morphological features of Fe₃O₄ nanoparticles (NPs) with its electrochemical properties. It was found that the co-precipitately synthesized Fe₃O₄ NPs are composed of 14-facet truncated octahedrons which contain 6 {100} and 8 {111} planes, and 26-facet polyhedrons which contain 6 {100}, 12 {110} and 8 {111} planes, indicating that the shape of NPs is changeable from 14-facet truncated octahedrons to 26-facet polyhedrons. As the anode for LIBs, it delivered a high initial discharge capacity of 1067 mA h g⁻¹, which could be attributed to their small size and the abundant exposure of edges and corners in the multi-faceted polyhedral structures, offering low-coordinated atoms that acted as active sites for lithium storage.

Introduction

Lithium ion batteries (LIBs) have been considered as the leading role in energy storage devices for a variety of electrical energy applications due to their high operational voltage, high-energy density, and long cycle life.^{1,2} The shape of nanocrystal of electrode material is an important issue because of its great influence to their physical and chemical properties.³⁻⁵ Up to now, a variety of nanocrystals with special shapes such as octahedral Co₃O₄ cages,⁶ rhombic dodecahedral Fe₃O₄ nanocrystals,⁷ hexagonal α-Fe₂O₃ nanorods⁸ and octahedral Mn₃O₄ nanoparticles⁹ have been synthesized for LIBs. Some studies have ever shown that the magnetic, optical, catalytic, and electrochemical properties of electrode materials can be strongly influenced by the shape, which governs the surface terminations and surface atomic arrangement.^{4,10-12} However, there are still rare reports about detailed characterization of crystal structure and its correlation with LIBs performance. It is necessary to acquire the information on the crystal shape and illustrate the shape-performance relationship in LIBs.

In recent years, Fe₃O₄ has been considered as a promising candidate as anode materials for LIBs because of its high theoretical capacities (924 mA h g⁻¹), nature abundance, inexpensive, and environmental benignity.¹³⁻¹⁵ As the crystal morphology of Fe₃O₄ plays a significant role in the electrochemical activity, Fe₃O₄ materials with different morphologies, including nanorings,¹⁶ nanospindles,¹⁷ nanorods,¹⁸ nanowires,¹⁹ hollow spheres,²⁰ nanoprisms,²¹ microflowers²², porous hollow microspheres²³ and clusters²⁴ have been synthesized. Among these different nanostructures, Fe₃O₄ nanoparticles are particularly suitable for electrodes of LIBs because of not only the size and surface effects,²⁵ which

provide large specific surface areas, short diffusion length and fast diffusion rates for Li ion and electrolyte,²⁶ but also the shape effect that holds great promise in boosting the LIB performance. The shape of NPs determines the arrangement of surface atoms, edges and corners are crucial to their electrochemical properties. For example, Cao *et al.*²⁷ prepared the Fe₃O₄ nanocrystals around 16 nm, which delivered an initial discharge capacity of 1200 mA h g⁻¹ at 0.2 C. Cheng *et al.*⁷ reported the synthesized of Fe₃O₄ nanocrystals with rhombic dodecahedral morphology, which exhibited an initial discharge capacity of 1147 mA h g⁻¹ and good rate capability at 1-4 C. Therefore, one of the strategies for high performance anode of LIB is to fabricate Fe₃O₄ nanoparticles with well-defined shape. On the other hand, to manipulate and optimize the electrochemical activities of Fe₃O₄ through shape design, an important step is to measure and characterize the shape in detail.

In this work, we present the fabrication and morphological investigation of the Fe₃O₄ NPs as well as their electrochemical activities. Fe₃O₄ NPs with diameters around 12 nm were synthesized by a coprecipitation method. The surface terminations and the shape of the particles were estimated by electron crystallography. It was found that the morphology of Fe₃O₄ NPs is a mixture of 14-facet truncated octahedral polyhedrons and 26-facet polyhedrons. In addition, the electrochemical performances of the NPs as anode materials for LIB in terms of charge/discharge capacity and cycle stability were evaluated.

Experimental

Synthesis of Fe₃O₄ nanoparticles

Magnetite NPs with the size around 12 nm were prepared by coprecipitating ferric and ferrous salts in alkaline solution under a non-oxidizing environment in the presence of polyethylene glycol (PEG). For a typical synthesis, 0.08 g $\text{FeCl}_2 \cdot 4\text{H}_2\text{O}$ and 0.2 g $\text{FeCl}_3 \cdot 6\text{H}_2\text{O}$ were homogeneously mixed with 200 mL distilled water. The reaction mixture was heated at 50 °C under a N_2 atmosphere. After the solution was sonicated for 10 min, ferric and ferrous salts were precipitated by adding dropwisely 10 ml of 8 M NH_4OH aqueous solution. The reaction was carried out at 50 °C for 30 min under magnetic stirring. The resulting Fe_3O_4 product was washed with distilled water and ethanol and finally dried under vacuum at 80 °C. The as-prepared product was dispersed in ethanol solution. A droplet of the suspension was deposited on a copper grid covered with a carbon film, followed by solvent evaporation before analysis.

Material Characterization

The morphologies, microstructures and compositions of the Fe_3O_4 NPs were characterized by field-emission scanning electron microscopy (FE-SEM, JSM-6330F), X-ray diffractometry (XRD, D8 Advance), transmission electron microscopy (TEM, JEM2010-HR, FEI Tecnai G² F30) and electron energy loss spectroscopy (EELS, Gatan Quantum 963). Synthesized Fe_3O_4 powder (as active material 80 wt %), acetylene black (as conductive agent 10 wt %), and polyvinylidene fluoride (PVDF as binder 10 wt %) were dissolved in N-methylpyrrolidone (NMP) to form a slurry. The slurry was then pressed onto a copper foil and dried in a vacuum oven at 100 °C for 12 h. The electrodes were pressed and cut into disks as anode. Coin cells (CR2032) were fabricated with as synthesized anode, lithium metal as counter electrode, Celgard 2400 as separator, and LiPF_6 (1M) in ethylene carbonate/dimethyl carbonate/diethyl carbonate (EC/DMC/DEC, 1:1:1 vol %) as the electrolyte. The cell was assembled in an Ar-filled glovebox. The rate capability and cycle life of the cells were tested in a potential window of 0.01~3 V (vs Li^+/Li) by a battery testing system (LAND CT 2001A). All of the specific capacities were calculated on the basis of the total weight of Fe_3O_4 (0.40 mg cm^{-2}).

Results and discussion

Polyhedral magnetite NPs were fabricated by coprecipitating ferric and ferrous salts in the presence of PEG. The structural and compositional features of the NPs were characterized by SEM, XRD, TEM, and EELS. Fig. 1(a) shows the X-ray diffraction (XRD) pattern of the Fe_3O_4 NPs. The diffraction peaks can be indexed as (220), (311), (400), (422), (511) and (400) reflections, which confirms the face-centered cubic (fcc) inverse spinel structure of magnetite (JCPDS No.65-3107). The morphology and microstructure of the Fe_3O_4 NPs were studied by SEM and TEM. Fig. 1(b) shows a typical SEM image of the Fe_3O_4 NPs. Most Fe_3O_4 NPs are uniformly distributed. Some aggregations of the NPs are also observed. Fig. 1(c) shows a typical TEM image of the Fe_3O_4 NPs. The roughly polyhedral shaped particles with average diameters of about 12 nm were observed. The selected-area electron diffraction (SAED) pattern (inset of Fig. 1(c)) can be indexed as 220, 113 and 400 diffractions of the fcc magnetite structure. In addition, the bright diffraction rings indicate that the Fe_3O_4 NPs were well crystallized. HRTEM image in Fig. 1(d) shows two randomly oriented Fe_3O_4 NPs. The interplanar spacing about 0.29 nm and 0.48 nm corresponding to the (220) and (111) lattice planes of

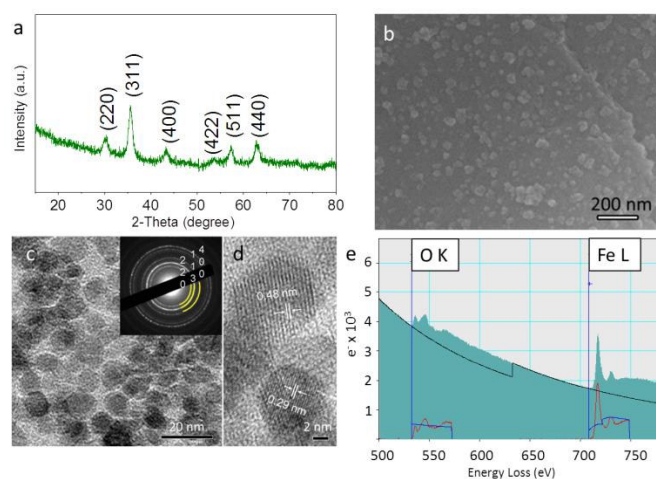


Fig. 1 (a) XRD patterns and (b) SEM image of Fe_3O_4 nanoparticles. (c) Bright field TEM image and the corresponding SAED pattern (inset) of Fe_3O_4 nanoparticles. (d) HRTEM image of two randomly oriented Fe_3O_4 nanoparticles. (e) EELS spectra of Fe_3O_4 nanoparticles with atomic ratios of Fe (44.04 %) and O (55.96 %). EELS was acquired at an energy range containing the Fe L_{2,3} and the O-K edges.

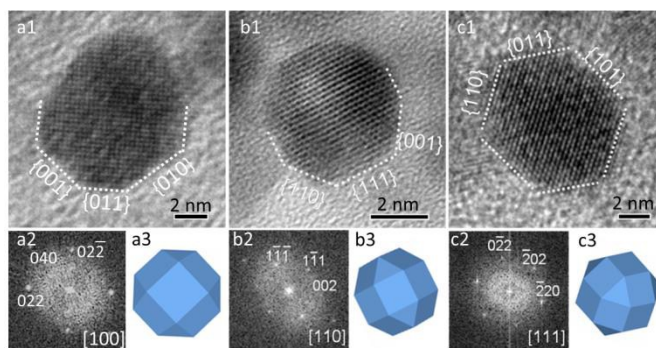


Fig. 2 HRTEM images of polyhedral Fe_3O_4 nanoparticles. (a1) Viewed along [100] with {020} and {022} enclosed facets. (b1) Viewed along [110] with {002}, {220} and {111} enclosed facets. (c1) Viewed along [111] with {220} enclosed facets. Panel (a2, b2, c2) are the Fast Fourier Transform (FFT) pattern corresponding to Panel (a1, b1, c1), respectively. Panel (a3, b3, c3) are the projected shapes of the 3D structural model along [100], [110] and [111], respectively.

the fcc structure of Fe_3O_4 is clearly identified. The chemical composition of Fe_3O_4 nanoparticles was characterized by electron energy-loss spectroscopy (EELS). As shown in Fig. 1(e), the characteristic O K-edge and the Fe L_{2,3}-edge were observed in the spectrum. The atomic ratio of Fe to O is determined to be 44.04:55.96, confirming that the obtained products are Fe_3O_4 crystals. In order to investigate the surface area of the Fe_3O_4 NPs, N_2 adsorption/desorption experiment at 77 K was carried out (as shown in Fig. S1). From the Brunauer–Emmett–Teller (BET) analysis the specific surface area of Fe_3O_4 NPs are calculated to be about 258 $\text{m}^2 \text{g}^{-1}$, indicating a small average size of the product.

To examine the particle shape and surface terminations, we performed HRTEM observation of various NPs with different orientations on the TEM grid. Fig. 2 shows some representative HRTEM images of NPs with different projections. Fourier filtering was used to extract the lattice fringes information. Surface terminations were determined while different crystal facets were oriented along the viewing directions. A close inspection of HRTEM images reveals that the Fe_3O_4 NPs are

usually in the form of square-like, octagonal-like, hexagonal-like and rhombic-like two-dimensional (2D) projected shapes. Fig. 2(a1) displays a HRTEM image of an individual NP with octagonal shape along $[100]$ direction. Well-resolved $\{022\}$ planes with a spacing of 0.29 nm is presented, indicating that the NP was sitting on a $\{100\}$ facet. In this orientation, four $\{010\}$ and $\{110\}$ facets are imaged edge-on. Fig. 2(b1) illustrates the $[110]$ projected image of an octagonal shaped particle. The lattice fringes of 0.48 nm and 0.41 nm corresponds to the interplanar distance of $\{111\}$ and $\{200\}$ lattice planes, respectively. In this case, $\{111\}$ and $\{001\}$ facets are viewed edge-on. Fig. 2(c1) shows the hexagonal projection of a NP viewed along $[111]$, where six $\{110\}$ facets are imaged edge on. The lattice planes with spacing of 0.29 nm can be indexed as $\{220\}$ facets. The six-fold symmetry revealed by FFT in panel c3 confirms the $[111]$ orientation of the particle, suggesting that the NP was sitting on a $\{111\}$ facet. Based on the crystallographic data provided by HRTEM images, a three-dimensional morphology of the hexagonal and octagonal shaped particles was proposed. An idealized geometrical structure is schematically provided in Fig. 3. The 26-facet rhombicuboctahedron shape that possesses 6 square $\{100\}$ facets, 12 square or rectangle $\{110\}$ facets and 8 triangular $\{111\}$ facets can be clearly identified. Each $\{111\}$ and $\{100\}$ facet is adjacent to three $\{110\}$ and four $\{110\}$ facets, respectively. There are 24 identical vertices and 52 edges on each rhombicuboctahedron, offering low-coordinated atoms that can have a strong impact on the chemical activity. In order to better understand this polyhedron structure, Fig. 3(b) presents the schematic illustrations of the 26-facet rhombicuboctahedron along three different orientations, showing how viewing along $[100]$, $[110]$ and $[111]$ directions accounts for different projected shapes. It can be seen that the projected contours of schematic model correspond well with the experimental images in Fig. 2, which suggest that the NPs with the co-presence of $\{100\}$, $\{110\}$ and $\{111\}$ facets should be attributed to 26-facet rhombicuboctahedron. In fact, $\gamma\text{-Fe}_2\text{O}_3$ with similar shapes ranging from 50 to 300 nm has been reported.^{28,29}

It should be noted that the hexagonal and octagonal projected shapes are not corresponding to the 26-facet rhombicuboctahedron morphology exclusively. Fig. 4 shows some hexagonal projections along $\langle 110 \rangle$ direction. As indicated by HRTEM, the surface terminations can be determined as $\{111\}$

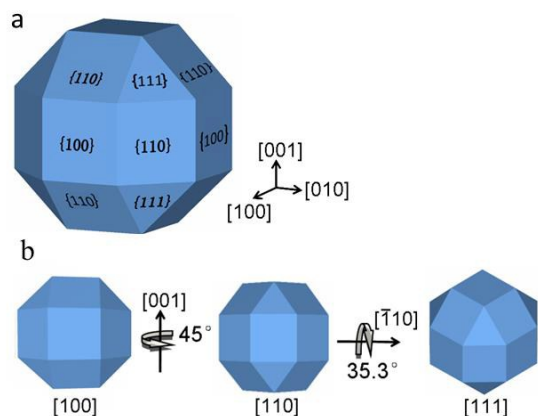


Fig. 3 (a) Geometrical model of an ideal 26-facet rhombicuboctahedron enclosed with $\{100\}$, $\{111\}$ and $\{110\}$ facets. (b) Schematic illustration showing how viewing along $[100]$, $[110]$ and $[111]$ directions accounts for the different projected shapes.

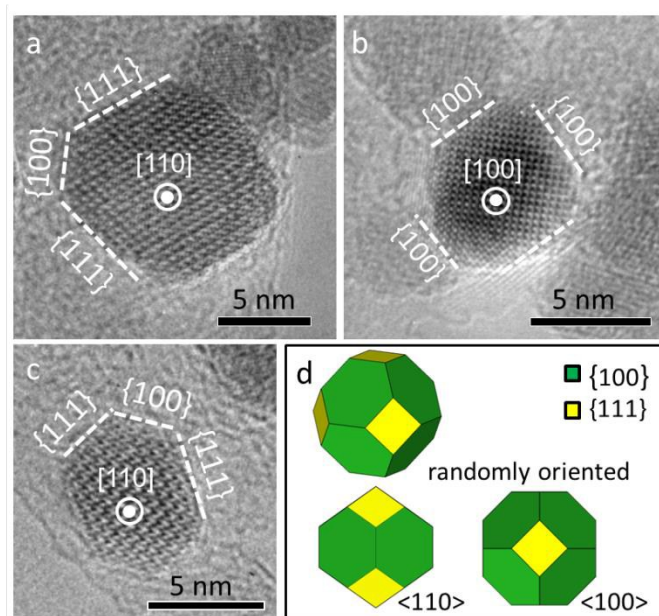


Fig. 4 HRTEM images of truncated octahedral Fe_3O_4 nanoparticles projected along (a) $\langle 110 \rangle$, (b) $\langle 100 \rangle$, and (c) $\langle 110 \rangle$ orientations. (d) Geometric models of the truncated octahedron enclosed with $\{100\}$ and $\{111\}$ facets. The green and yellow colors represent $\{111\}$ and $\{100\}$ facets, respectively.

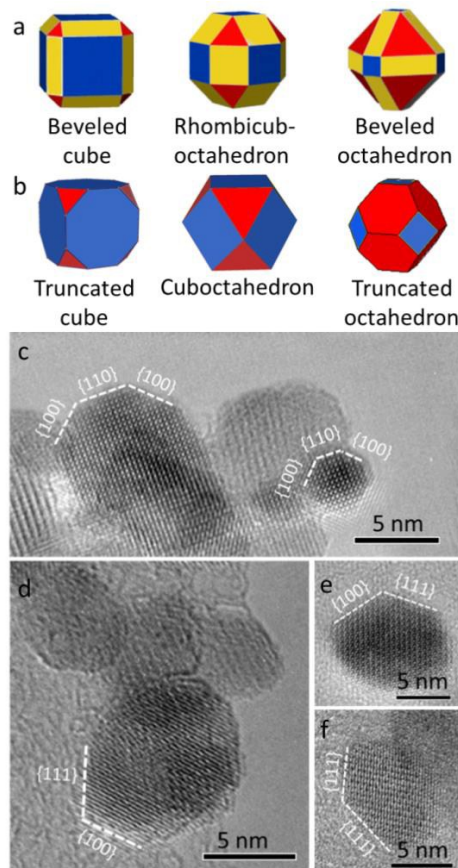


Fig. 5 Schematic models of series of (a) 26-facet polyhedrons enclosed with $\{100\}$, $\{111\}$ and $\{110\}$ facets, and (b) 14-facet polyhedrons enclosed with $\{100\}$ and $\{111\}$ facets. $\{110\}$, $\{111\}$ and $\{100\}$ facets are coloured yellow, red and blue, respectively. (c-f) HRTEM images of polyhedral Fe_3O_4 nanoparticles with distorted octagonal-like, distorted hexagonal-like, rhombic-like and rhomboid-like projected contours, respectively.

and {100} facets. In addition, the 2D projection taken along the $\langle 100 \rangle$ zone axis exhibited a truncated square shape. The results indicated that the NPs exclusively enclosed by {111} and {100} facets should be attributed to truncated octahedron, which contains 8 {111}, 6 {100} exposed facets and 24 vertices as well as 36 edges. The different projected shapes are related to the same morphology observed along different crystallographic orientations, which is in accordance with the scheme in Fig. 4(d).

In general, the 26-facet rhombicuboctahedron shape can be seen as truncating the corners and edges of a regular octahedron, while the 14-facet truncated octahedron can be viewed as truncating along {100} facets of a regular octahedron.³⁰ Therefore, different degrees of truncation will eventually lead to the formation of a series of morphologies. For example, beveled cube and beveled octahedron can be related to rhombicuboctahedron with different degrees of face-directed truncation, while truncated cube and cuboctahedron can be related to truncated octahedron with different degrees of edge-directed truncation.³¹ Hence, the rest observed projections such as distorted hexagonal-like, distorted octagonal-like, rhombic-like and rhomboid-like projections that terminated by {100}, {110} and {111} exposed facets should also be attributed to the 26-facet polyhedron and/or 14-facet truncated octahedron morphologies. Representative TEM images are selected and displayed in Fig. 5. As the projection contours vary depending on the direction that the NP is viewed, various projected shapes can be resulted from viewing along different crystallographic directions. Although the particles shown in Fig. 5 are different in shape, all of them are enclosed with three low-energy surfaces {100}, {110}, and {111}. According to TEM investigation of about 900 individual particles in the copper grid, the population distribution of each exposed facets was statistically obtained. It was found that the percentage of {100}, {110}, and {111} is calculated to be 28.0 %, 34.7 %, and 37.3 %, respectively.

From all the above discussion, the morphologies of the as-synthesized nanoparticles should be consisted of 14-facet truncated octahedrons and 26-facet polyhedrons. Taking into account that the surface energy among different planes of a fcc structure follows the order: $\gamma\{111\} < \gamma\{100\} < \gamma\{110\}$, a possible growth mechanism of the NPs is proposed. Fig. 6 demonstrated the shape transformation process of the polyhedral Fe_3O_4 NPs. In the early stage of crystal growth, the Fe_3O_4 nuclei tend to form a seed with octahedral shape bounded by the most stable {111} planes.³² Meanwhile, PEG as a capping agent would preferentially adsorb on the relatively high

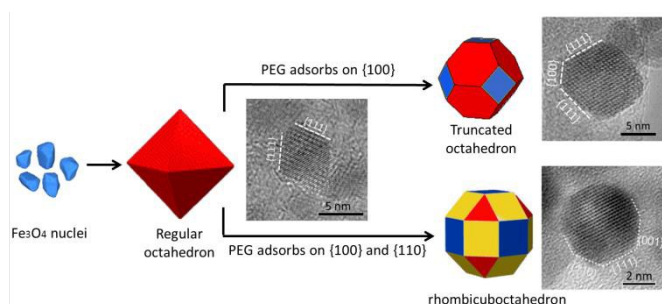


Fig. 6. Schematic illustration of the proposed growth mechanism that lead to the formation of truncated octahedral and rhombicuboctahedral Fe_3O_4 nanoparticles. {110}, {111} and {100} facets are coloured yellow, red and blue, respectively. The presence of PEG transforms the regular octahedron into the truncated octahedron and rhombicuboctahedron.

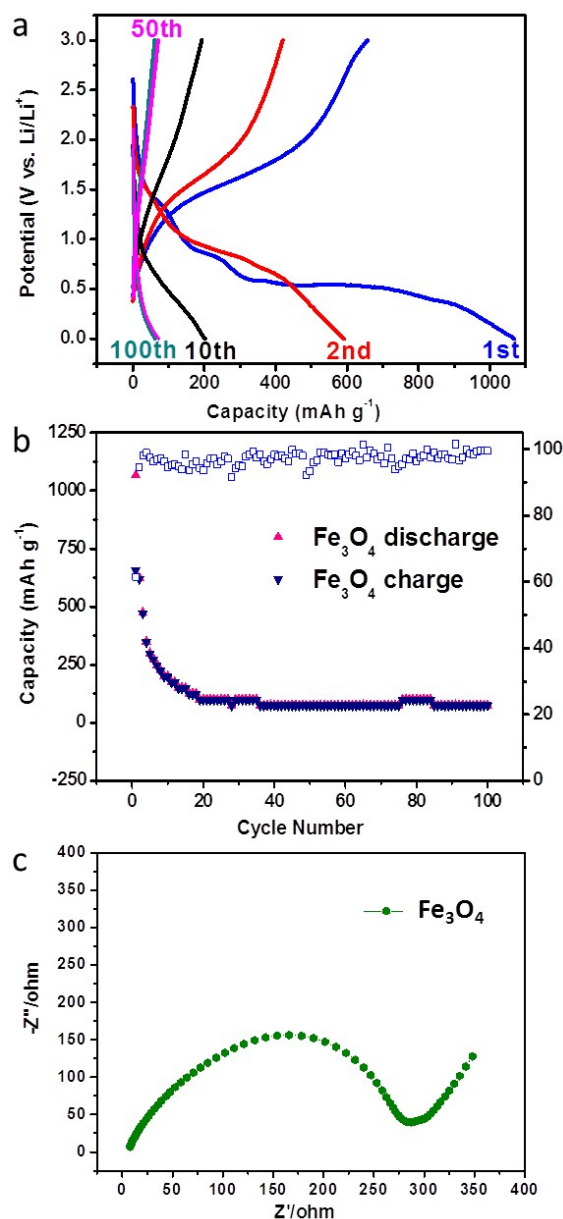


Fig. 7. (a) Charge-discharge voltage profiles of the Fe_3O_4 anode at a current density of 100 mA g^{-1} . (b) Cycling performance of the Fe_3O_4 anodes charged and discharged at a current of 100 mA g^{-1} over 100 cycles. (c) Nyquist plots of the Fe_3O_4 electrodes at fresh coin cells over the frequency range from 100 kHz to 0.01 Hz.

energy {110} and {100} surfaces of Fe_3O_4 , leading to the slow growth of {110} and {100} planes on the seed. In the process of crystal formation, the octahedron seed gradually evolves while PEG limits the growth rates of {100} planes, resulting in 14-facet truncated octahedral shapes with both the {100} and {111} surfaces well developed. With increasing reaction time, the particle would grow further to form a 26-facet polyhedron as a result of the slow growth of both {100} and {110} planes. Hence, the final shape of Fe_3O_4 NPs observed in TEM images is a mixture of series of 14-facet truncated octahedrons and 26-facet polyhedrons, all of which contain abundant low-coordinated atoms located at edges and corners that can act as active sites for chemical reactions.

The electrochemical performance for LIBs was studied for the investigation of correlation between the crystal morphology and electrochemical properties. The galvanostatic charge-discharge measurements were carried out at a current density of 0.1 A g⁻¹ between 0.001 and 3.00 V for 100 cycles (Fig. 7(a)). The first discharge and charge capacities of the polyhedral Fe₃O₄ NPs are 1067 and 657 mA h g⁻¹, respectively, indicating a high reversibility. The capacity loss after the first cycle's discharge can be attributed to the irreversible reactions occurred during the formation of the solid electrolyte interface (SEI) layer. The polyhedral Fe₃O₄ NPs exhibited a higher initial specific discharge capacity than that described in the literatures, such as Fe₃O₄ nanoparticle cluster anode (about 850 mA h g⁻¹ at 100 mA g⁻¹),²⁴ hollow Fe₃O₄ nanoparticle anode (about 800 mA h g⁻¹ at 100 mA g⁻¹),³³ Fe₃O₄ microspheres (about 910 mA h g⁻¹ at 100 mA g⁻¹),³⁴ Fe₃O₄@C nanoparticles (926 mA h g⁻¹ at 60 mA g⁻¹),³⁵ commercial Fe₃O₄ particles (about 790 mAh g⁻¹ at 100 mA g⁻¹)³⁶, and are also comparable to other Fe₃O₄ nanostructure and Fe₃O₄ nanocomposite electrode materials, such as Fe₃O₄ submicron spheroids (1332 mA h g⁻¹ at 0.2 C),³⁷ 3D porous nano-Ni/Fe₃O₄ composite film (1324.3 mA h g⁻¹ at 0.1 C)³⁸ and hierarchical Fe₃O₄ microsphere/graphene nanosheet composite (1336.4 mA h g⁻¹ at 200 mA h g⁻¹).³⁹ The improved initial discharge capacity of polyhedral Fe₃O₄ NPs can be ascribed to the following reasons: first, the polyhedral shape of the NPs provides abundant low-coordinated atoms located on the edges and corners, serving as extra active sites for conversion reaction. Second, the high specific surface area resulted from the small size increases the contact area between active material and electrolyte. Fig. 7(b) shows the coulombic efficiency and cycling performance of the Fe₃O₄ NPs. A coulombic efficiency of 62 % was obtained at first cycle after which increased to 94.6 % and approximately 100 % in following cycles. For the stability, the discharge capacities of the Fe₃O₄ anode at the 2nd and 10th cycles were 625 and 200 mA h g⁻¹, respectively, and then decreased to 75 mA h g⁻¹ after 100 cycles, indicating a poor electrochemical stability, which should be due to the aggregation and large volume expansion of the NPs during electrochemical cycling.⁴⁰ To investigate the morphological features of the NPs after discharge-charge cycling, TEM of Fe₃O₄ NPs after 20 cycles was shown in Fig. S2 (SI). The NPs become larger and densely packed. In addition, most NPs are connected to each other, some even fuse together to form bigger particles. From the results, it is confirmed that the aggregation and volume changes of the Fe₃O₄ NPs are obvious during discharge-charge process, resulting in the poor cycling stability. Electrochemical impedance spectroscopy (EIS) analysis was also conducted on the Fe₃O₄ electrode. Fig. 7(c) shows the Nyquist plot of the Fe₃O₄ electrodes at fresh coin cells over the frequency range from 100 kHz to 0.01 Hz. The electrodes present a semicircle in the middle-high frequency region and a sloped straight line in the low frequency region. The charge-transfer resistance of the Fe₃O₄ electrode is 284 Ω, which indicated the inherent low electronic and ionic conductivity. Although the polyhedral Fe₃O₄ NPs exhibited a high initial specific capacity, the poor cycling stability hinders their practical application in LIBs. Integrating Fe₃O₄ NPs with carbon materials to form composite is in experimental progress to improve their cycling stability.

Conclusions

In summary, we have investigated the shape of Fe₃O₄ nanoparticles synthesized by a coprecipitation method and their electrochemical performances. Transmission electron

microscopy analysis suggested that the resulting morphologies are composed of 14-facet truncated octahedrons and 26-facet polyhedrons with different degrees of truncation along {110} and {100} planes. The results implied that the morphology of nanoparticles can evolve from regular octahedrons to 14-facet truncated octahedrons, and then further grow to form a diversity of 26-facet polyhedrons, while polyethylene glycol plays an important role in tuning the shape. Galvanostatic charge-discharge measurements indicate that the Fe₃O₄ nanoparticles exhibited a relatively high initial discharge capacity, which should be attributed to their small size and the abundant exposure of low-coordinated atoms at the edges and corners that act as active-sites. These findings will be contributed to clarify the shape-dependent electrochemical properties of Fe₃O₄ nanoparticles. It is expected that the lithium storage capability could be further enhanced by optimizing the shape and structure of Fe₃O₄ nanoparticles.

Acknowledgements

We acknowledge the financial support of this work by the Natural Science Foundations of China (21273290, 21476271 and J1103305), the Research Fund for the Doctoral Program of Higher Education of China (20120171110043) and the Integration of Production and Research Projects of the Ministry and Guangdong Province (2011B090400618).

Notes and references

^a KLGHEI of Environment and Energy Chemistry, MOE of the Key Laboratory of Bioinorganic and Synthetic Chemistry, School of Chemistry and Chemical Engineering, Sun Yat-Sen University, Guangzhou 510275, People's Republic of China. E-mail: chedhx@mail.sysu.edu.cn; ce04lxh@mail.sysu.edu.cn; Fax: +86-20-84112245; Tel: +86-20-84110071

^b Instrumental Analysis and Research Centre, Sun Yat-Sen University, Guangzhou 510275, People's Republic of China.

Electronic Supplementary Information (ESI) available: [details of any supplementary information available should be included here]. See DOI: 10.1039/b000000x/

1. M. S. Balogun, M. H. Yu, C. Li, T. Zhai, Y. Liu, X. H. Lu and Y. X. Tong, *J. Mater. Chem. A*, 2014, **2**, 10825-10829.
2. K. Zhong, Y. Cui, X. D. Xia, J. J. Xue, P. Liu and Y. X. Tong, *J. Power Sources*, 2014, **250**, 296-305.
3. J. M. Yang, Q. Liu and W. Y. Sun, *Micropor. Mesopor. Mater.*, 2014, **190**, 26-31.
4. T. Ming, W. Feng, Q. Tang, F. Wang, L. Sun, J. Wang and C. Yan, *J. Am. Chem. Soc.*, 2009, **131**, 16350-16351.
5. H. G. Yang, C. H. Sun, S. Z. Qiao, J. Zou, G. Liu, S. C. Smith, H. M. Cheng and G. Q. Lu, *Nature*, 2008, **453**, 638-641.
6. X. Wang, L. Yu, X. L. Wu, F. Yuan, Y. G. Guo, Y. Ma and J. Yao, *J. Phys. Chem. C*, 2009, **113**, 15553-15558.
7. X. L. Cheng, J. S. Jiang, D. M. Jiang and Z. J. Zhao, *J. Phys. Chem. C*, 2014, **118**, 12588-12598.
8. Y. M. Lin, P. R. Abel, A. Heller and C. B. Mullins, *J. Phys. Chem. Lett.*, 2011, **2**, 2885-2891.
9. S. Z. Huang, J. Jin, Y. Cai, Y. Li, H. Y. Tan, H. E. Wang, G. Van Tendeloo and B. L. Su, *Nanoscale*, 2014, **6**, 6819-6827.
10. Y. Xiong and Y. Xia, *Adv. Mater.*, 2007, **19**, 3385-3391.

11. L. Zhao, H. Zhang, J. Tang, S. Song and F. Cao, *Mater. Lett.*, 2009, **63**, 307-309.
12. T. K. Sau and A. L. Rogach, *Adv. Mater.*, 2010, **22**, 1781-1804.
13. C. Yang, J. Wu and Y. Hou, *Chem. Commun.*, 2011, **47**, 5130-5141.
14. X. Zhao, D. Xia and K. Zheng, *ACS Appl. Mater. Interfaces*, 2012, **4**, 1350-1356.
15. Q. Qu, S. Yang and X. Feng, *Adv. Mater.*, 2011, **23**, 5574-5580.
16. L. Wang, J. Liang, Y. Zhu, T. Mei, X. Zhang, Q. Yang and Y. Qian, *Nanoscale*, 2013, **5**, 3627-3631.
17. W. M. Zhang, X. L. Wu, J. S. Hu, Y. G. Guo and L. J. Wan, *Adv. Funct. Mater.*, 2008, **18**, 3941-3946.
18. P. Tartaj and J. M. Amarilla, *J. Power Sources*, 2011, **196**, 2164-2170.
19. T. Muraliganth, A. Vadivel Murugan and A. Manthiram, *Chem. Commun.*, 2009, 7360-7362.
20. H. Geng, Q. Zhou, Y. Pan, H. Gu and J. Zheng, *Nanoscale*, 2014, **6**, 3889-3894.
21. Y. Zeng, R. Hao, B. Xing, Y. Hou and Z. Xu, *Chem. Commun.*, 2010, **46**, 3920-3922.
22. S. Jin, H. Deng, D. Long, X. Liu, L. Zhan, X. Liang, W. Qiao and L. Ling, *J. Power Sources*, 2011, **196**, 3887-3893.
23. B. Wang, H. B. Wu, L. Zhang and X. W. Lou, *Angew. Chem. Int. Ed.*, 2013, **52**, 4165-4168.
24. S. H. Lee, S. H. Yu, J. E. Lee, A. Jin, D. J. Lee, N. Lee, H. Jo, K. Shin, T. Y. Ahn, Y. W. Kim, H. Choe, Y. E. Sung and T. Hyeon, *Nano Lett.*, 2013, **13**, 4249-4256.
25. F. Niederdraenk, K. Seufert, A. Stahl, R. S. Bhalerao-Panajkar, S. Marathe, S. K. Kulkarni, R. B. Neder and C. Kumpf, *Physical Chemistry Chemical Physics*, 2011, **13**, 498-505.
26. J. Jiang, Y. Li, J. Liu, X. Huang, C. Yuan and X. W. Lou, *Adv. Mater.*, 2012, **24**, 5166-5180.
27. H. Cao, R. Liang, D. Qian, J. Shao and M. Qu, *J. Phys. Chem. C*, 2011, **115**, 24688-24695.
28. N. Zhao, W. Ma, Z. Cui, W. Song, C. Xu and M. Gao, *ACS Nano*, 2009, **3**, 1775-1780.
29. S. Inamdar, H. S. Choi, M. S. Kim, K. Chaudhari and J. S. Yu, *CrystEngComm*, 2012, **14**, 7009-7014.
30. M. Leng, C. Yu and C. Wang, *CrystEngComm*, 2012, **14**, 8454-8461.
31. S. Alvarez, *Dalton Trans.*, 2005, 2209-2233.
32. Z. L. Wang, *J. Phys. Chem. B*, 2000, **104**, 1153-1175.
33. D. Chen, G. Ji, Y. Ma, J. Y. Lee and J. Lu, *ACS Appl. Mater. Interfaces*, 2011, **3**, 3078-3083.
34. Y. Gan, H. Gu, H. Xiao, Y. Xia, X. Tao, H. Huang, J. Du, L. Xu and W. Zhang, *New J. Chem.*, 2014, **38**, 2428-2434.
35. J. Liu, J. Ni, Y. Zhao, H. Wang and L. Gao, *J. Mater. Chem. A*, 2013, **1**, 12879-12884.
36. J. E. Lee, S. H. Yu, D. J. Lee, D. C. Lee, S. I. Han, Y. E. Sung and T. Hyeon, *Energy Environm. Sci.*, 2012, **5**, 9528-9533.
37. S. Q. Wang, J. Y. Zhang and C. H. Chen, *J. Power Sources*, 2010, **195**, 5379-5381.
38. Q. Q. Xiong, J. P. Tu, Y. Lu, J. Chen, Y. X. Yu, X. L. Wang and C. D. Gu, *J. Mater. Chem.*, 2012, **22**, 18639-18645.
39. T. Q. Wang, X. L. Wang, Y. Lu, Q. Q. Xiong, X. Y. Zhao, J. B. Cai, S. Huang, C. D. Gu and J. P. Tu, *RSC Adv.*, 2014, **4**, 322-330.
40. C. L. Liang, T. Zhai, W. Wang, J. Chen, W. X. Zhao, X. H. Lu, Y. X. Tong, *J. Mater. Chem. A*, 2014, **2**, 7214-7220.